Dynamic and structural responses of a submerged floating tunnel under extreme wave conditions

Chungkuk Jin and MooHyun Kim[*]

Department of Ocean Engineering, Texas A&M University, College Station, TX, USA

Abstract. The dynamic and structural responses of a 1000-m long circular submerged floating tunnel (SFT) with both ends fixed under survival irregular-wave excitations are investigated. The floater-mooring nonlinear and elastic coupled dynamics are modeled by a time-domain numerical simulation program, OrcaFlex. Two configurations of mooring lines i.e., vertical mooring (VM) and inclined mooring (IM), and four different buoyancy-weight ratios (BWRs) are selected to compare their global performances. The result of modal analysis is included to investigate the role of the respective natural frequencies and elastic modes. The effects of various submergence depths are also checked. The envelopes of the maximum/minimum horizontal and vertical responses, accelerations, mooring tensions, and shear forces/bending moments of the entire SFT along the longitudinal direction are obtained. In addition, at the mid-section, the time series and the corresponding spectra of those parameters are also presented and analyzed. The pros and cons of the two mooring shapes and high or low BWR values are systematically analyzed and discussed. It is demonstrated that the time-domain numerical simulation of the real system including nonlinear hydro-elastic dynamics coupled with nonlinear mooring dynamics is a good method to determine various design parameters.

Keywords: submerged floating tunnel (SFT); hydro-elasticity; coupled dynamics; wet natural modes; dynamic/structural responses; irregular waves; vertical/inclined mooring; mooring tension; buoyancy weight ratio (BWR); shear force; bending moment

1. Introduction

A submerged floating tunnel (SFT) is a novel structure to cross deep waterway, such as river, canal, bay, fjord, or strait (Paik *et al.* 2004, Ge *et al.* 2010). The SFT is mainly comprised of floating tunnel and mooring/anchoring system. The tunnel is located underwater at a certain depth and has positive net buoyancy balanced by the anchoring system (Di Pilato *et al.* 2008, Long *et al.* 2009, Cifuentes *et al.* 2015). Although SFTs have been proposed as an effective traffic solution to cross waterways, such as the Hogsfjord in Norway, the Strait of Messina in Italy, and the Funka Bay in Japan (Skorpa 1989, Fujii 1996, Remseth *et al.* 1999, Faggiano *et al.* 2001), there is no real construction of the SFT in the world yet (Lu *et al.* 2011, Lee *et al.* 2017). The first construction of the SFT is currently considered by Norwegian Public Road Administration (NPRA) in 2016 (Ghimire and Prakash 2017).

∗Corresponding author, Professor, E-mail: m-kim3@tamu.edu

The SFT has several advantages over bridges or traditional underground/immersed tunnels. Particularly, bridges and underground/immersed tunnels are vulnerable to earthquakes. The bridge is also susceptible to extreme wind and wave loads and ship passage (Long *et al.* 2009). However, the SFT is less vulnerable to the extreme wind/wave loads and the seismic load by floating and deeply submerged. The closed (capsuled) hull can also be directly applicable to the hyper-loop concept in the future. The global performance of the SFT depends on various design parameters, such as submergence depth, buoyancy-weight ratio (BWR), and the configuration/interval of mooring lines. In general, to warrant ship passage and minimize wave effects, the submergence depth greater than 25-30 m is recommended (Indridason 2013).

The dynamic and structural analyses of SFTs have been undertaken by several researchers. Wahyuni *et al.* (2012) studied the dynamic response of SFTs under hydrodynamic, current, and earthquake conditions. In their research, dynamic responses increase as various loads act together, and among the environmental loads, wave loads were the most important. Several researchers have conducted studies for a small, rigid segment of the SFT. Kunisu *et al.* (1994) investigated the configuration of SFT mooring lines in a regular wave condition. They concluded that vertical mooring lines lead to larger sway natural period than inclined mooring lines. In addition, the snap load occurred for inclined mooring lines due to sudden transitions from slack condition to taut condition, which can be controlled by increasing the BWR. Hong and Ge (2010) carried out experiments, and they found that a change in the BWR results in the variation of dynamic responses. They also calculated shear forces and bending moments with different end boundary conditions. Slack phenomena and snap loads of inclined mooring lines were also reported by Lu *et al.* (2011), in which the increased wave height and decreased BWR lead to more slack phenomena, and mooring tension significantly increases due to the associated snap loading. Oh *et al.* (2013) conducted scaled experiments in regular wave conditions at different BWRs, water depths, and mooring shapes. Their results were compared with the results of time-domain simulations by Cifuentes *et al.* (2015) and Lee *et al.* (2017), where the simulation results reasonably coincided with the experimental results. In addition, they showed that inclined mooring lines exhibited much smaller SFT dynamic responses than vertical mooring lines. Seo *et al.* (2015) also verified the trend of experimental results with simplified analysis under regular wave conditions.

On the other hand, several researchers investigated the dynamics of long SFTs including elasticity under wave excitations. Long *et al.* (2009) investigated the effect of tunnel length and BWR on SFT dynamic responses, where the BWR change contributed more to the change of dynamics than the tunnel length with the given end boundary condition. Mazzolani *et al.* (2008) conducted structural analyses of the SFT with different configurations of mooring lines. Chamelia *et al.* (2015) carried out numerical simulations to figure out the influence of waves and currents on the SFT at different inclination angles and numbers of mooring lines. Finally, authors (Jin *et al.* (2017) carried out numerical simulations for the SFT including hydro-elasticity under survival-wave and seismic excitations. The configuration of mooring lines was found to be critical in reducing SFT responses for the respective wave and seismic excitations.

In this research, the floater-mooring-coupled nonlinear time-domain numerical simulations of an 1000-m-span SFT are performed by utilizing the commercial program, OrcaFlex. A survival random-wave condition is used to analyze the corresponding dynamic and structural responses. Two configurations of mooring lines, four BWRs, and three submergence depths are studied to find the trend/sensitivity of SFT global performance with those design parameters. Longitudinal elasticity is considered with fixed-end conditions. Modal analysis of the entire system is conducted to obtain natural frequencies and corresponding modes. SFT dynamic responses, mooring tensions,

and shear forces/bending moments are analyzed, and relevant physics are discussed through the respective time series and spectra.

2. Configuration of submerged floating tunnel

Fig. 1 shows 3D schematic drawing of single segment of the SFT including mooring lines. The structural parameters of the tunnel and mooring lines are summarized in Table 1. The tunnel's entire length and outer diameter are 1,000 m and 23 m, respectively. For simplicity, the tunnel is modeled as a cylindrical outer shell only since, in this paper, we only focus on the global dynamic performance of the entire system. The equivalent bending stiffness of the simple-cylinder model can be determined from more complex FE (finite element) program of more realistic system. Steel is chosen for the outer shell of the tunnel, and different thicknesses are designated to match the BWRs. In addition, since the thickness of the tunnel changes the cross-sectional area and the second moment of area, different values of axial stiffness, bending stiffness, and torsional stiffness are used for different BWRs. Both ends of the tunnel are assumed to be fixed with high translational, bending, and torsional stiffness. Different BWRs of 1.1, 1.3, 1.5, and 1.7 and water depths of 80 m, 100 m, and 120 m are selected as design parameters.

Two configurations of mooring lines are chosen i.e., vertical mooring lines perpendicular to seabed (VM) and inclined mooring lines that are 60 degrees inclined to seabed (IM) (Oh *et al.* 2013, Cifuentes *et al.* 2015, Lee *et al.* 2017). Chain properties are exploited to model the mooring lines. The equivalent-bar diameter is 0.18 m and chain density is 7,820 kg/m^3. The axial stiffness of chain is 2.77×10^9 N. Different longitudinal distances between mooring lines (mooring intervals) are selected for VM and IM. While the mooring interval of IM is 50 meters, that of VM is 25 meters to match the total number of mooring lines for comparison purposes. For simplicity, the flat seabed is also assumed. However, it can easily be varied for variable seabed when necessary. The mooring-line length of each VM is 38.5 m (Line #1 and #2) while IM has longer and shorter mooring lines, and their lengths are 51.1 m (Line #1 and #2) and 37.8 m (Line #3 and #4), respectively.

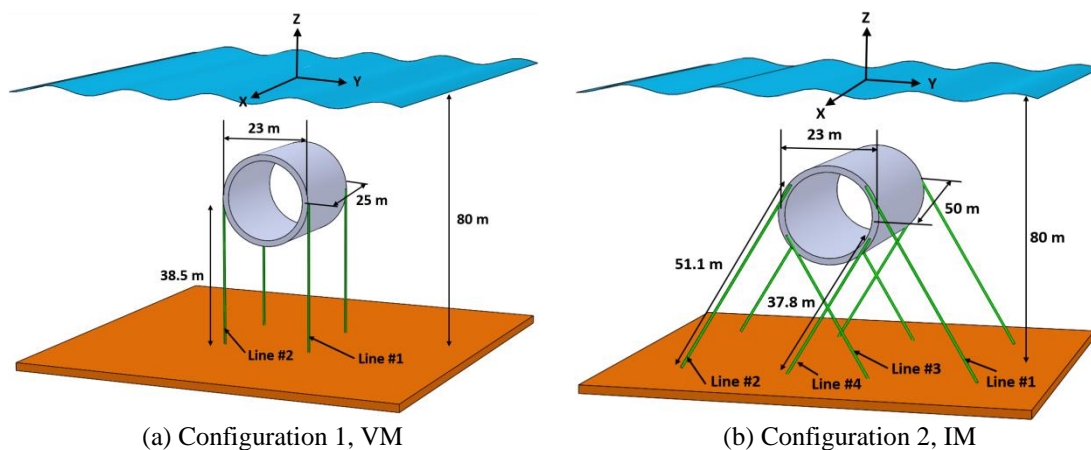(a) Configuration 1, VM   (b) Configuration 2, IM

Fig. 1 3D schematic drawing of each section of SFT and configuration of mooring lines

Table 1 Structural parameters of the tunnel and mooring lines (bs=bending stiffness)

Structure	Item	Unit	Value
Tunnel	BWR		1.1, 1.3, 1.5, 1.7
	Outer diameter	m	23
	Length	m	1000
	Thickness, bs of outer shell at BWR 1.1	m, N-m^2	0.70, 6.50×10^{14}
	Thickness, bs of outer shell at BWR 1.3	m, N-m^2	0.59, 5.56×10^{14}
	Thickness, bs of outer shell at BWR 1.5	m, N-m^2	0.51, 4.85×10^{14}
	Thickness, bs of outer shell at BWR 1.7	m, N-m^2	0.45, 4.30×10^{14}
	Young's modulus	N/m^2	2.12×10^{11}
Mooring lines	Bar diameter	m	0.18
	Length of VM	m	38.5
	Length of IM #1 and #2	m	51.1
	Length of IM #3 and #4	m	37.8
	Density	kg/m^3	7,820
	Axial stiffness	N	2.77×10^9

Table 2 Natural frequencies and the corresponding directions of mode shapes of the entire system as a function of BWR up to 2nd mode (Y: horizontal (transverse) direction, Z: vertical direction)

BWR	SFT-VM		SFT-IM	
	Mode shape	Natural Frequency (rad/s)	Mode shape	Natural Frequency (rad/s)
1.1	Y	0.642	Y	1.383
	Y	1.746	Y	2.122
	Z	2.732	Z	2.215
	Z	3.177	Z	2.700
1.3	Y	0.635	Y	1.434
	Y	1.683	Y	2.118
	Z	2.827	Z	2.333
	Z	3.227	Z	2.800
1.5	Y	0.627	Y	1.463
	Y	1.625	Y	2.096
	Z	2.904	Z	2.398
	Z	3.268	Z	2.825
1.7	Y	0.621	Y	1.486
	Y	1.574	Y	2.075
	Z	2.968	Z	2.451
	Z	3.301	Z	2.844

Table 2 provides the wet natural frequencies and the corresponding directional modes for the entire system. The typical feature of VM is that it is very stiff in the vertical direction but soft in the horizontal (transverse) direction. Therefore, the VM shows smaller natural frequencies in the horizontal direction than IM, while the opposite is true for natural frequencies in the vertical direction.

3. Numerical analysis in time domain

Time-domain simulations are performed to analyze dynamic and structural responses of the SFT under wave excitations. In this research, time-domain simulations of the SFT are done by a commercial program, OrcaFlex. The equations of motions of the tunnel section for horizontal and vertical motions in time domain are expressed as follows

$$\left[M + M^a\left(\infty\right) \right]\ddot{X} + K_h X = F_w + F_d + F_m \tag{1}$$

where M and $M^a\left(\infty\right)$ are mass and added mass at infinite frequency, K_h is the hydrostatic restoring coefficient, which is zero for horizontal and vertical motions of submerged floating structures, F_w is the wave-induced inertia force, F_d is the wave-motion-induced nonlinear drag force, and F_m is the mooring force. $\ddot{X}$ and X represent acceleration and displacement of the SFT section, respectively. In the vertical equation of motion, the constant buoyancy force is balanced by the weight of the tunnel and the vertical component of initial mooring tension. Morison equation for a moving body, which is comprised of linear inertia and quadratic drag forces, is utilized to estimate the hydrodynamic loads on the tunnel and mooring lines. Total hydrodynamic load per unit length for a cylinder is given by

$$\mathbf{F} = C_m \rho \frac{\pi D^2}{4}\dot{\mathbf{u}} - C_a \rho \frac{\pi D^2}{4}\ddot{\mathbf{X}} + \frac{1}{2}\rho C_d D \left|\mathbf{u} - \dot{\mathbf{X}}\right|\left(\mathbf{u} - \dot{\mathbf{X}}\right) \tag{2}$$

where ρ is density of sea-water, D is the outer diameter of a cylinder, $C_m (=1+C_a)$ is the inertia coefficient, C_a is added mass coefficient, C_d is the drag coefficient. $\dot{\mathbf{X}}$ denotes velocity vector of the structure, and $\dot{\mathbf{u}}$ and $\mathbf{u}$ represent acceleration and velocity vectors of a fluid particle. The inertia coefficient used for the tunnel and mooring lines is 2 ($C_a = 1$) (Faltinsen 1993). The constant drag coefficient of 0.55 for the tunnel is selected from experimental results based on Reynold number and relative surface roughness (ESDU, 1980). The drag coefficient of mooring lines is 2.4 assuming stud-less chain (DNV, 2010).

As for wave kinematics, Wheeler stretching method is applied to Airy linear wave theory for better estimation of fluid velocity and acceleration (Cifuentes and Kim 2017), which can be used for both regular and irregular waves (Wheeler 1969). For example, in Airy wave theory, the horizontal particle velocity can be expressed as

$$u(x,z,t) = \omega\zeta_a \frac{\cosh\left[k\left(z+h\right)\right]}{\sinh\left(kh\right)}\sin\left(\omega t - kx\right) \tag{3}$$

where ω is wave angular frequency, ζ_a is wave amplitude, h is water depth, and k is wave number. In this case, the depth-attenuation factor, $\cosh\left[k\left(z+h\right)\right]/\sinh\left(kh\right)$, exponentially decays with submergence depth, while it becomes unrealistically large above mean water level.

Wheeler stretching method suggests replacing z with z_1 that is a function of instantaneous wave elevation, ζ.

$$z_1(x,t) = \frac{h(h+z)}{h+\zeta(x,t)} - h$$

(4)

It has been reported that Wheeler stretching method can better fit to the measured wave kinematics than the direct use of linear wave theory (Longridge *et al.* 1996).

The tunnel and mooring lines are modelled as a series of lumped mass connected by linear and rotational springs. The slender line is divided into nodes and segments. Mass, buoyancy, drag, and other properties are lumped at each node, and nodes are connected by massless spring representing axial, bending, and torsional properties (Orcina 2015). Since two end points of SFT are fixed to the earth, only elastic dynamic responses occur through the entire length. At each section, we can observe horizontal and vertical dynamic responses.

4. Results and discussion

4.1 Static analysis

In this section, the results of static analyses for water depth of 80 m are presented to describe not only the relationship among vertical displacement, mooring tension, shear force, and bending moment but also the effect of the BWR in the static condition. Fig. 2 shows the vertical static displacement of the tunnel as a function of the BWR. The tunnels are slightly curved upward due to excessive net buoyancy and fixed boundary conditions at both ends. The increase of the BWR contributes to larger static displacement and curvature due to larger net buoyancy. The static vertical displacement of VM is less than that of IM because its vertical stiffness is larger.

Fig. 3 shows the initial tension of mooring lines as function of the BWR. The trend is similar to that of static vertical displacement (Fig. 2), as can intuitively expected.
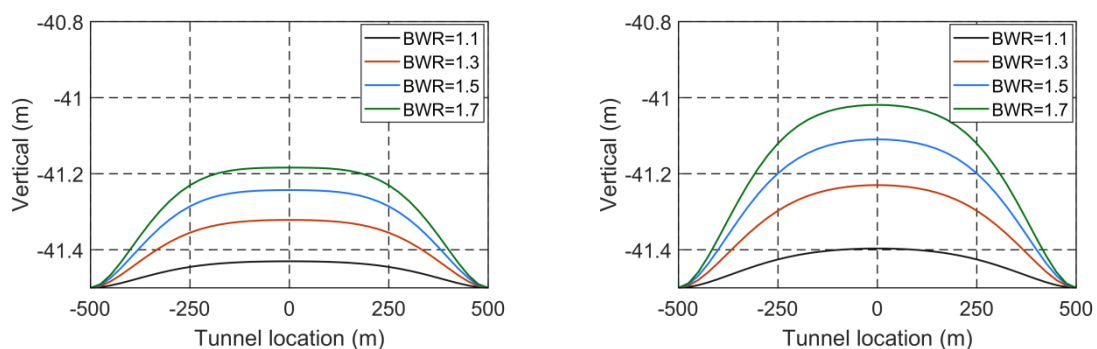

Fig. 2 Envelopes of vertical static displacement of the tunnel for VM (left) and IM (right) as a function of the BWR
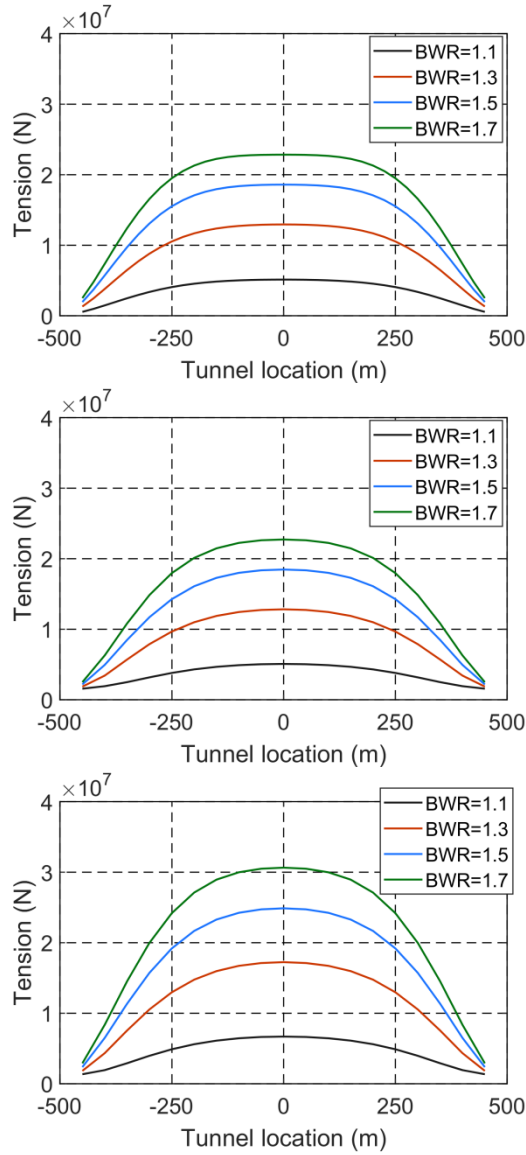
Fig. 3 Envelopes of static tension of mooring lines (Line #1 and #2) of VM (top), long mooring lines (Line #1 and #2) of IM (middle), and short mooring lines (Line #3 and #4) of IM (bottom) as a function of the BWR

    The increase of the BWR directly results in larger vertical static displacements and initial tensions. Since the maximum vertical displacement occurs in the middle span, the maximum initial mooring tension is also observed there. In case of IM, shorter lines have higher initial tension than longer lines due to their higher stiffness. The maximum static tension of VM is smaller than that of IM because its interval is half of IM's interval, and IM can additionally provide much larger restoring force in the horizontal direction than VM, which can be a major benefit of IM.
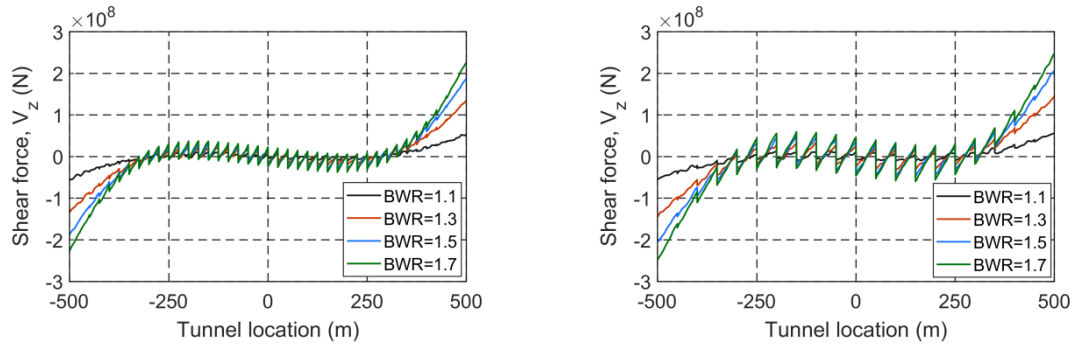
Fig. 4 Envelopes of static shear force of VM (left) and IM (right)
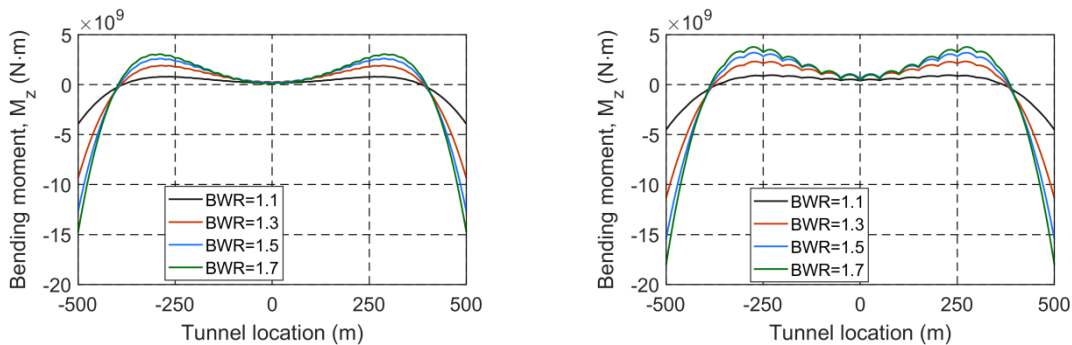
Fig. 5 Envelopes of static bending moment of VM (left) and IM (right)

Figs. 4 and 5 show the shear force and bending moment in the static condition. As described before, clamped conditions are used for both ends of the SFT. Therefore, the maximum shear force and bending moment are observed there. Shear forces are to smoothly change along the longitudinal direction of the tunnel due to uniformly distributed net buoyancy forces along the tunnel, but sudden saw-tooth-like decreases of shear forces happen at the mooring locations due to their 'pull-down' forces. The maximum bending moments occur at both ends, as expected, and the smallest bending moment is seen near the middle of the tunnel due to the minimal curvature there. The shear forces and bending moments generally increase with the BWR, and the rates of increases are particularly noticeable near both ends i.e., large BWR should be avoided in view of the sharp increase of shear force and bending moment at both ends. Larger fluctuations of shear forces and bending moments are observed in case of IM compared to VM since the distance between mooring in IM is twice that of VM i.e., more burden on each mooring location.

5.2 Dynamic analysis under wave excitations

In this section, the dynamic-analysis results under random-wave excitations are presented. The wave-induced dynamic loading can be significant in long waves particularly when the submergence depth of SFT is not deep enough. To check its survivability, an extreme wave condition is considered. The envelopes of horizontal and vertical motions of the tunnel as well as

dynamic mooring-line tensions are included. Both time series and spectra are presented and analyzed.

JONSWAP wave spectrum is used with significant wave height of 11.6 m, peak period of 15.1 sec, and enhancement parameter of 3.3. Wave heading is set to be perpendicular to the longitudinal direction of the tunnel, which is to be the most critical case. 3-hour simulations are performed for every case. Random waves are generated by the superposition of 100 component waves with randomly perturbed intervals to prevent signal repetition (Kim and Yue 1991). The lowest and highest cut-off frequencies of the input spectrum are 0.21 rad/s and 4.16 rad/s, respectively.

Figs. 6-8 show the envelopes (maxima and minima) of wave-induced horizontal and vertical motions of the tunnel and mooring-line tensions along the longitudinal direction with varying BWRs (water depth=80 m). The maximum horizontal and vertical elastic motions occur at the middle segment of the tunnel since both ends are clamped. The horizontal motions of VM are generally larger than those of IM at the same BWR because the horizontal lowest-mode natural frequency of VM is much closer to the input-wave energy than that of IM. This phenomenon is caused by the configuration of mooring line since vertical mooring hardly provides strong restoring force in the horizontal direction. In case of VM, the dynamic horizontal motions become larger with increasing BWR since the lowest-mode natural frequencies get closer to incident wave spectrum. Whereas, the opposite trend is observed for IM due to the shift of the lowest natural frequency farther away from wave spectrum with increasing BWR.
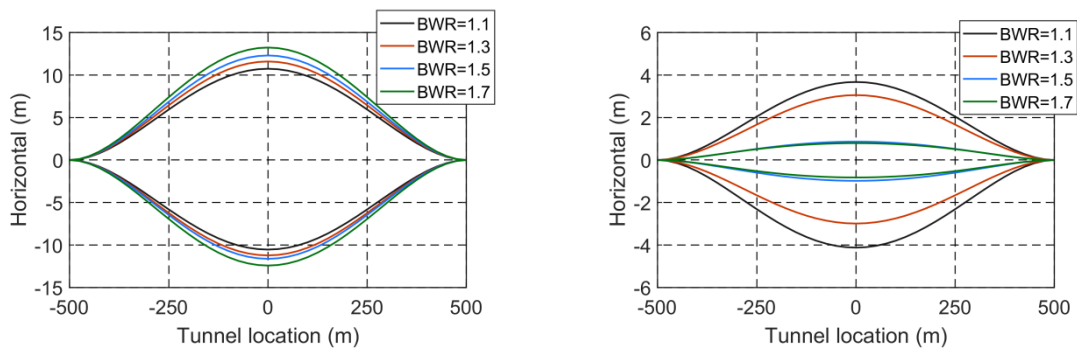

Fig. 6 Envelopes of horizontal motion for VM (left) and IM (right)
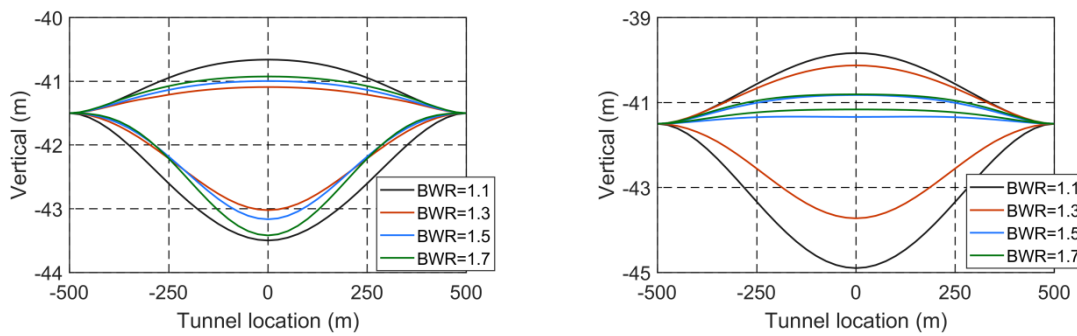

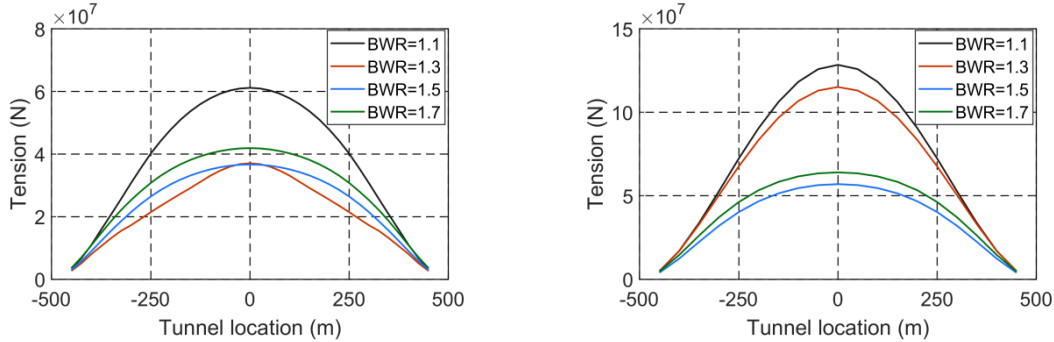Fig. 7 Envelopes of vertical motion for VM (left) and IM (right)

Fig. 8 Envelopes of mooring tension for VM (Line #1) (left) and IM (Line #4) (right)

In case of the envelopes of vertical motions, both VM and IM show the largest motion amplitudes at BWR=1.1 as shown in Fig. 7. As for IM, the envelope amplitudes monotonically decrease with increasing BWR. However, in case of VM, the envelope amplitudes of BWR=1.7 and 1.5 are greater than that of BWR=1.3 because larger horizontal motions also contribute to the additional vertical motions through the set-down effect of an inverted pendulum.

The trend of VM tensions tends to follow that of vertical motions, while the trend of IM tensions tends to follow that of both horizontal and vertical motions The maximum tension of IM (Line # 4) is much higher than that of VM (Line #1) at the same BWR as shown in Fig. 8. This can be explained by that the mooring interval of IM is twice that of VM which results in more burden to each mooring station. Another factor is the slack mooring phenomenon. One side of IM can be slack and, in this case, the tensions of taut mooring lines increase significantly to support the entire system. However, the VM shows uniform tension distribution between the two taut vertical lines and the burden is equally shared. Next, let us investigate the actual time series and spectra of horizontal and vertical SFT responses and mooring tensions.

Figs. 9-12 show the time series and spectra of horizontal and vertical motions and mooring tensions at the mid-section of the tunnel for BWR= 1.1 and 1.7 (water depth=80 m). In case of horizontal motions of VM (Figs. 9(a) and 10(a)), the first small peak corresponds to the peak frequency of input wave spectrum and the second large peak occurs at its lowest natural frequency. On the other hand, the IM's lowest natural frequencies for horizontal motions (Fig. 11(a)) are relatively higher, near 1.38 and 1.49 rad/s, thus we see in Fig. 11(a) negligible effect of resonance there. The overall horizontal-motion magnitudes of IM are much smaller than those of VM, as also observed in the previous figures, which demonstrates that IM is much more efficient in restricting horizontal dynamic responses. It is also seen that the horizontal motion of VM remains similar for BWR=1.1 and 1.7 (Figs. 9(a) and 10(a)) but that of IM is reduced to one quarter with increasing BWR from 1.1 to 1.7 (Figs. 11(a) and 12(a)).

In Fig. 9b, the vertical motion of VM has two prominent peaks, one at low frequency less than 0.2 rad/s and the other at high frequency around 1.28 rad/s. In case of the latter, it is mainly caused by the set-down effect of inverted pendulum. Therefore, for each positive and negative horizontal motions, we see negative vertical motions, which thus becomes double frequency of horizontal motions. On the other hand, the high energy in low frequency range is caused by two factors; one is the beat phenomenon (slowly varying amplitude modulation by two closely-spaced peaks in

horizontal/vertical motions) and the other is due to nonlinear phenomenon associated with the slack (instantaneous decrease of vertical stiffness) mooring lines. We also see the similar trend in the case of VM BWR=1.7 (Fig. 10(b)). IM at BWR=1.1 (Fig. 11(b)) also has similar trend by the same reasons. However, in case of IM at BWR=1.7 (Fig. 12(b)), the horizontal motion is peaked at the maximum of incident wave spectrum and there is a small peak near the lowest natural frequency of 1.49 rad/s. Since two peaks are widely separated, there is no beat phenomenon. Also, the horizontal-motion amplitudes are small, and thus the corresponding set-down effect of vertical motion at double frequency is also minimal, as can be clearly seen in Fig. 12(b). In this case, there are negligible vertical responses in low frequency range, contrasting to other cases, since small vertical motions make mooring lines remain taut without slacking, which can be double-checked by a careful observation of mooring-line behaviors in a separate animation.

(a) Time series of horizontal motion

(b) Spectrum of horizontal motion

(c) Time series of vertical motion

(d) Spectrum of vertical motion

(e) Time series of mooring tension (Line #1)

(f) Spectrum of mooring tension (Line #1)
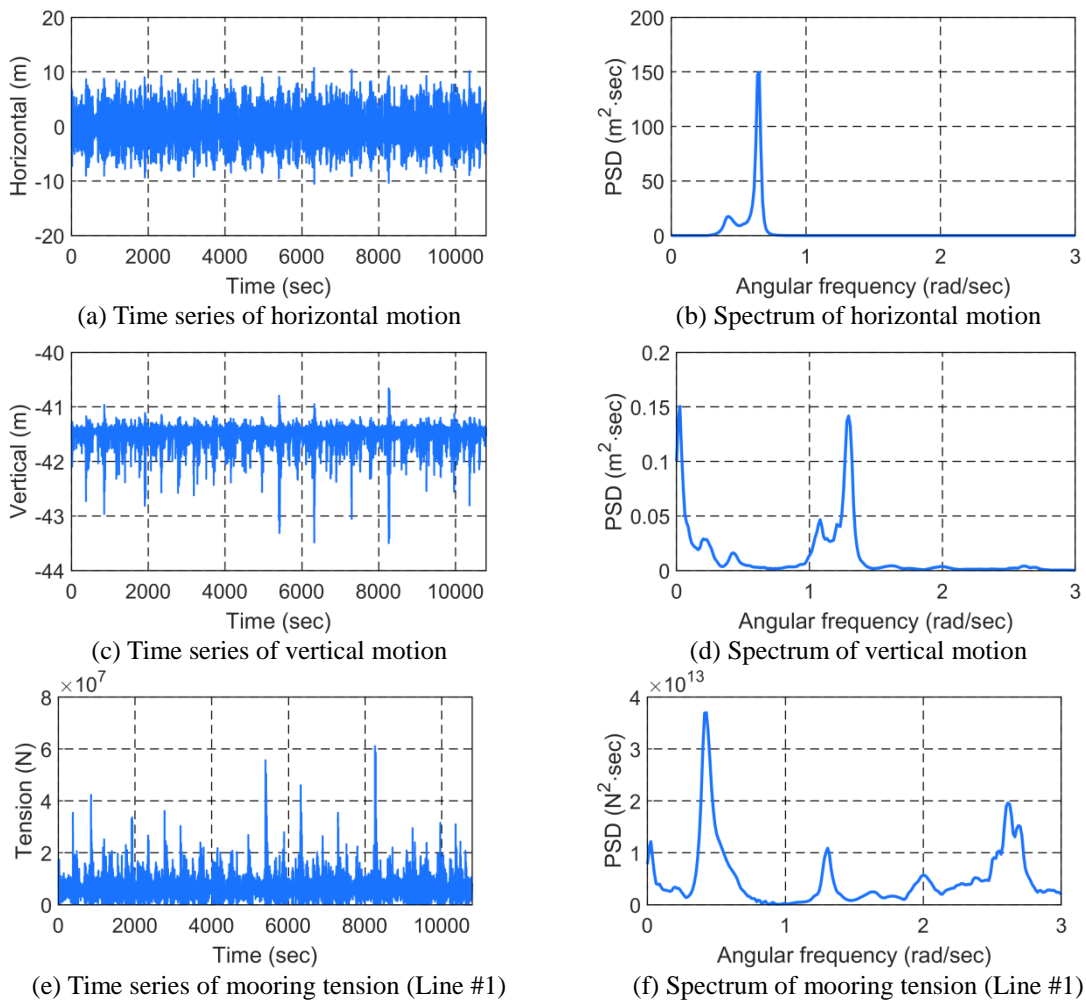
Fig. 9 Time series of VM at the BWR of 1.1 and corresponding spectra

(a) Time series of horizontal motion

(b) Spectrum of horizontal motion

(c) Time series of vertical motion

(d) Spectrum of vertical motion

(e) Time series of mooring tension (Line #1)
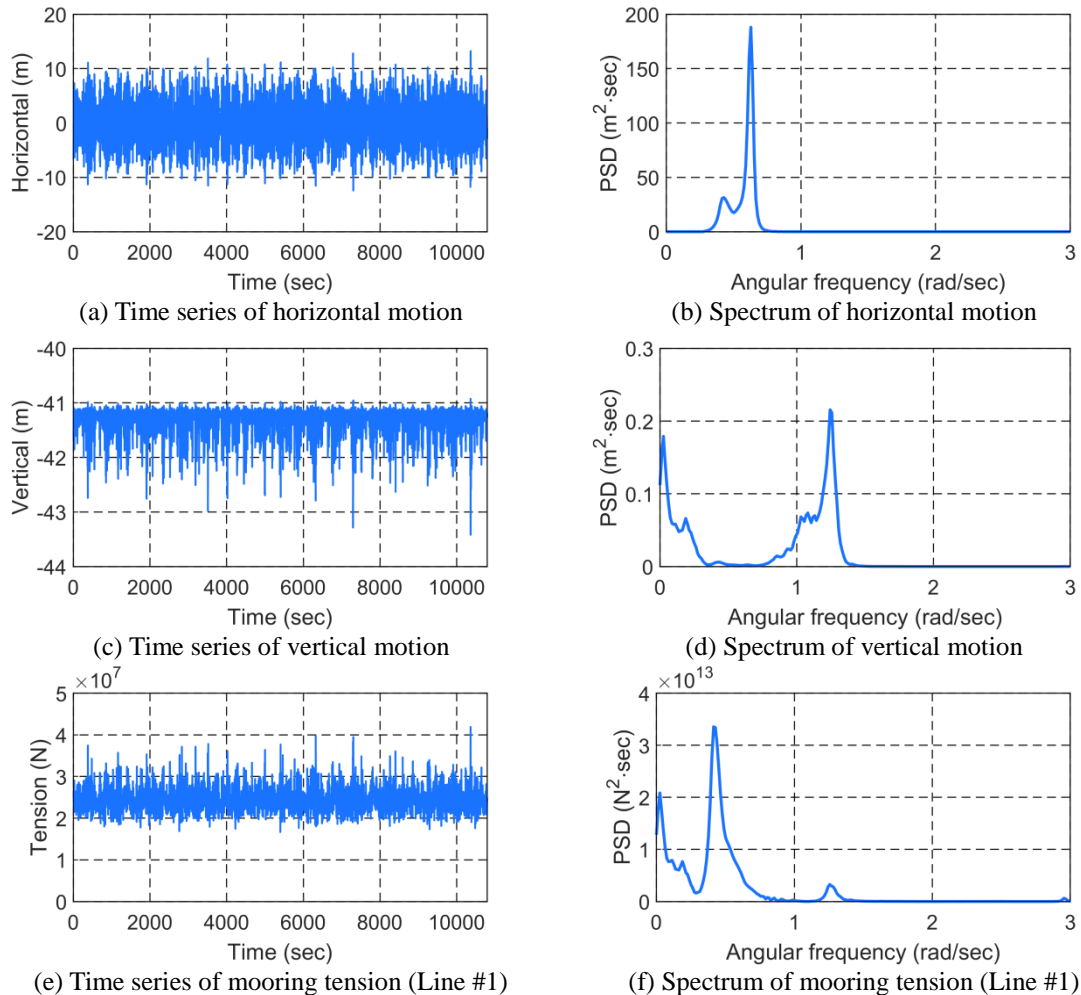
(f) Spectrum of mooring tension (Line #1)

Fig. 10 Time series of VM at the BWR of 1.7 and corresponding spectra

In Fig. 9(c), VM and BWR=1.1, we have peaks of mooring tensions at the peaks of horizontal and vertical motions. There also exists a significant peak near the lowest vertical-elastic-motion natural frequency of 2.73 rad/s. In Fig. 10(c), VM and BWR=1.7, we observe similar trend as Fig. 9(c) except the absence of high-frequency resonance peak since the lowest elastic natural frequency is shifted to 2.97 rad/s with BWR=1.7. In Fig. 11(c), IM and BWR=1.1, the mooring tension spectrum is more widely spread as a result of more complicated coupled and nonlinear phenomena. In Fig. 12(c), IM and BWR=1.7, the peaks of mooring tensions more clearly follow those of horizontal (1.49 rad/s) and vertical (2.45 rad/s) resonant elastic responses. When the mooring tension time series of BWR=1.1 are inspected with enlarged portion of the time series, it is seen that the mooring can be slack while the tunnel undergoes large downward motion. Shortly after that, the mooring lines experience sharply increased snap loading when the tunnel bounces back and reaches the maximum upward motion. The snap-loading effects are significantly decreased when BWR=1.7.

In Fig. 12, to observe the effect of increasing submergence depth of the tunnel, we increased both water depth and submergence depth by 20 m and 40 m while keeping the same mooring system. Considering the fast decay of wave induced forces with depth, we intuitively expect that all the wave related dynamic effects are to be decreased accordingly, which can actually be observed both in time series and spectra of horizontal and vertical responses and mooring tensions regardless of mooring types. Therefore, submergence depth is the key parameter in reducing wave-induced dynamic responses and the corresponding mooring tensions. Both in VM and IM, the static tension is increased with higher BWR but the dynamic tension is reduced with higher BWR. So, the optimal BWR can be searched through case studies. For the present case, BWR=1.3 for VM and 1.5 for IM show the best dynamic-tension performance.

(a) Time series of horizontal motion

(b) Spectrum of horizontal motion

(c) Time series of vertical motion

(d) Spectrum of vertical motion

(e) Time series of mooring tension (Line #4)

(f) Spectrum of mooring tension (Line #4)
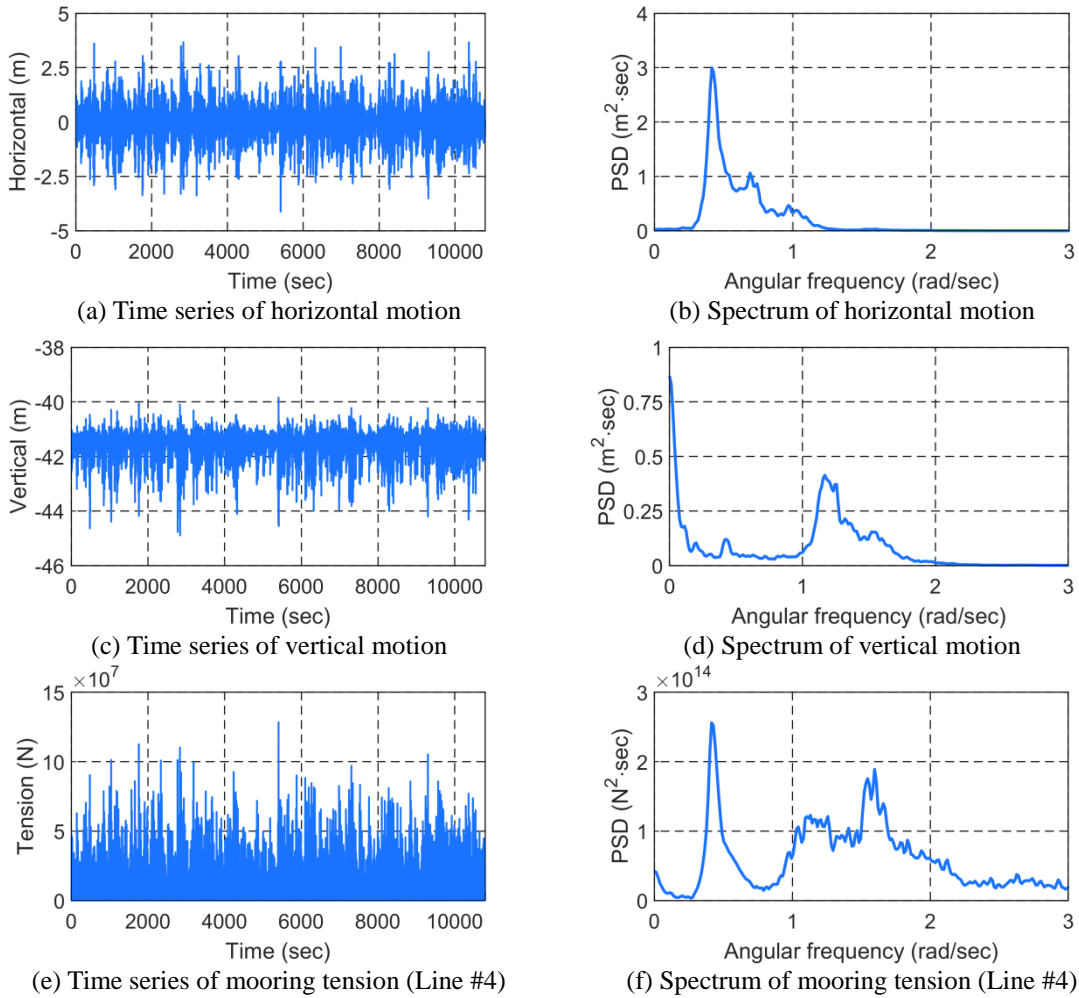
Fig. 11 Time series of IM at the BWR of 1.1 and corresponding spectra

(a) Time series of horizontal motion

(b) Spectrum of horizontal motion

(c) Time series of vertical motion

(d) Spectrum of vertical motion

(e) Time series of mooring tension (Line #4)

(f) Spectrum of mooring tension (Line #4)
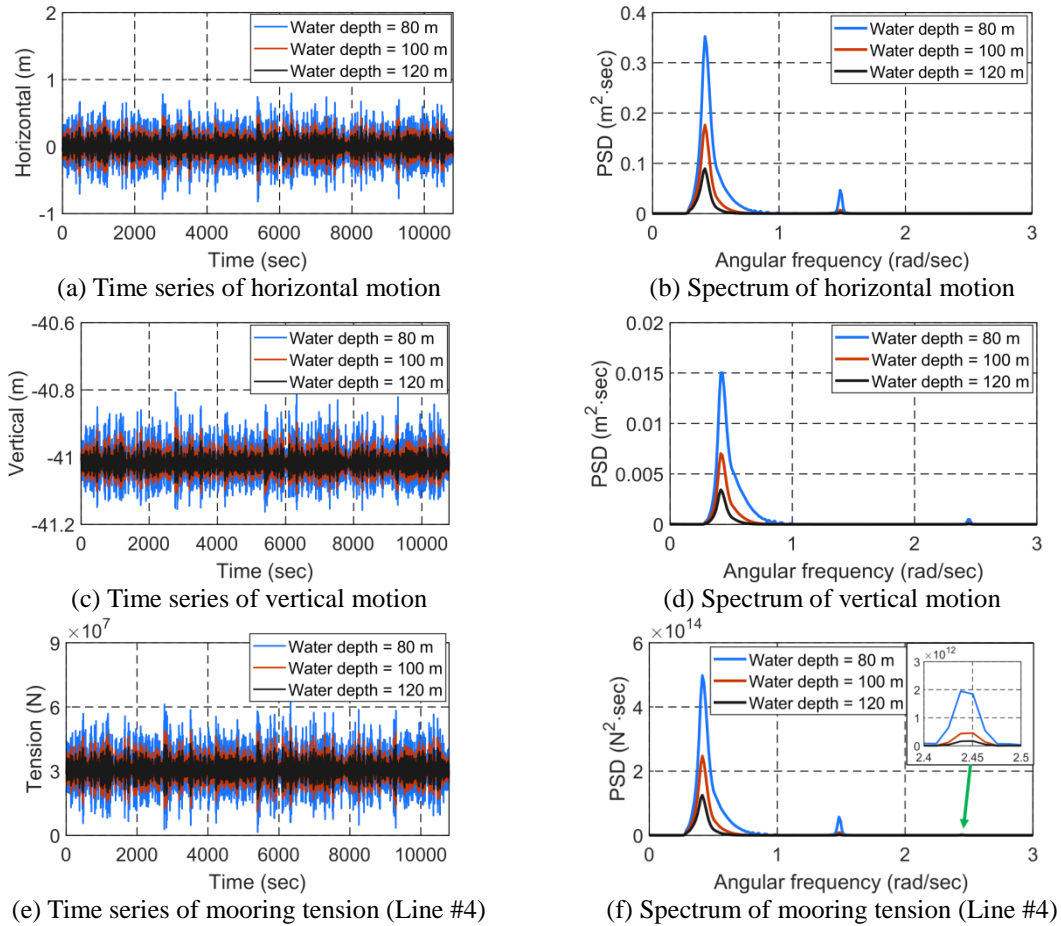
Fig. 12 Time series of IM at the BWR of 1.7 and corresponding spectra

5.3 Structural analysis under wave excitations

In this section, the results of structural analysis under wave excitations are presented. The envelopes of sectional maximum shear forces and bending moments in horizontal and vertical directions are given in Figs. 13 and 15. In addition, the time series and spectra of those are also plotted in Figs. 14 and 16.

From Fig. 13, the sectional maximum shear forces both in horizontal and vertical directions occur at the end locations of the tunnel since both ends are clamped (fixed-fixed condition). As pointed out before, the pattern of vertical-shear-force variation along the longitudinal direction is similar between VM and IM but the local saw-tooth-like variation of IM is larger because the mooring interval is longer in IM. Particularly, the dynamic horizontal shear forces of IM vary a lot depending on the applied BWRs compared to VM. The horizontal shear force of VM is larger than that of IM due to larger horizontal motions and associated inertia forces.
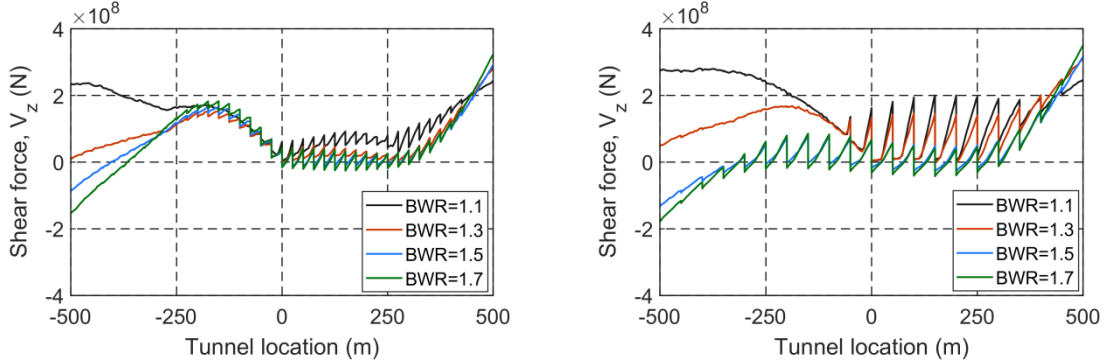
(a) Envelope of the maximum shear force in the vertical direction (VM)

(b) Envelope of the maximum shear force in the vertical direction (IM)
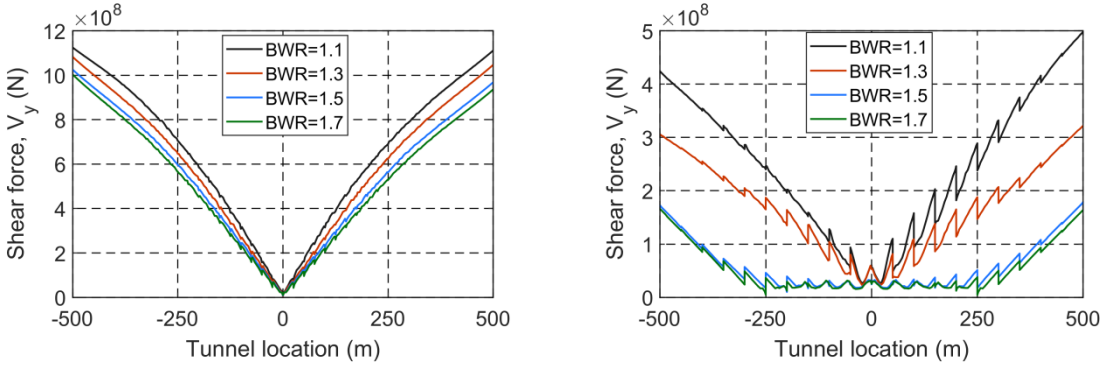
(c) Envelope of the maximum shear force in the horizontal direction (VM)

(d) Envelope of the maximum shear force in the horizontal direction (IM)

Fig. 13 Envelopes of the maximum shear force of the tunnel for VM and IM

In Fig. 14(a) at the mid-section of VM, the vertical mean (static) shear force of BWR=1.7 is larger than that of BWR=1.1 but the opposite is true for its dynamic shear force. Particularly, highly amplified instantaneous negative shear forces can happen for BWR=1.1, as can be seen in Figs. 14(a) and 14(e) time series. However, in horizontal shear forces of VM, the overall dynamic amplification of BWR=1.7 case is much larger, as can be clarified from the corresponding spectrum. In case of IM of Fig.14, the trend of vertical shear force is similar to that of VM but its dynamic horizontal shear forces of BWR=1.7 are smaller than those of BWR=1.1 due to more effective limitations of horizontal responses.

Finally, Fig.15 shows the envelopes of bending moments along the length in vertical and horizontal directions. We clearly see that the maximum bending moments occur at the end positions. In VM case, the maximum vertical bending moments increase a lot with decreasing BWRs, but horizontal components are much less sensitive to the change of BWRs. However, in case of IM, both vertical and horizontal maximum bending moments increase significantly with decreasing BWRs.
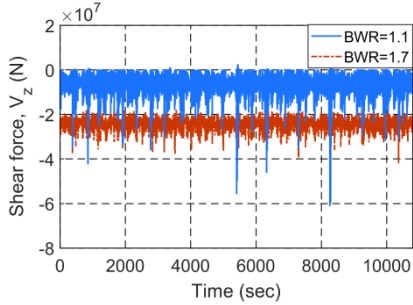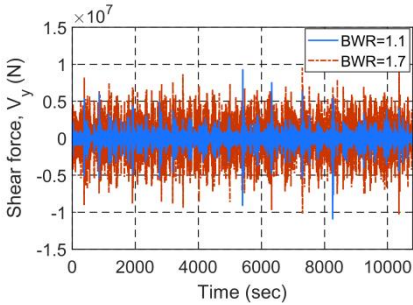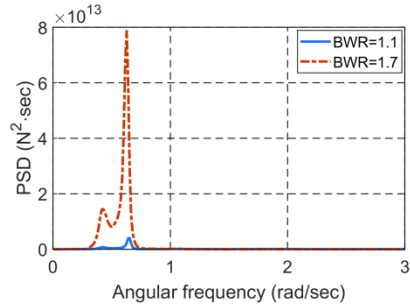
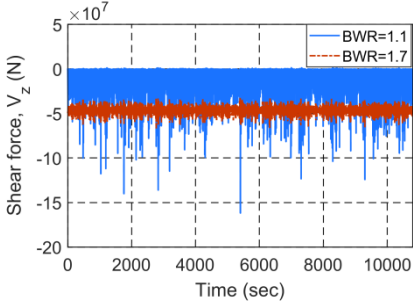(a) Time series of shear force in the vertical direction (VM)
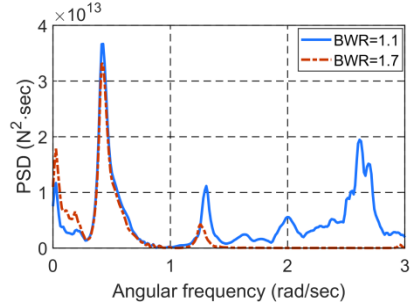
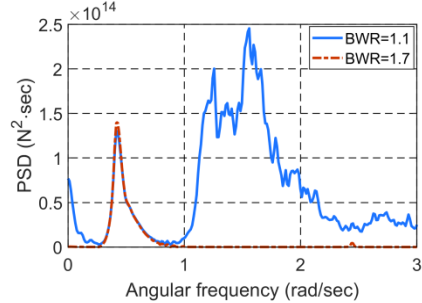(b) Spectrum of shear force in the vertical direction (VM)

(c) Time series of shear force in the horizontal direction (VM)
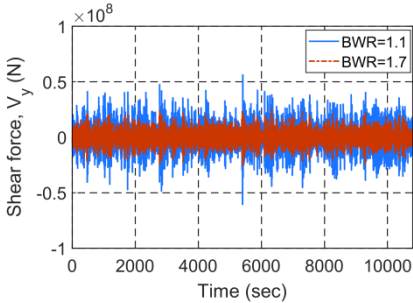
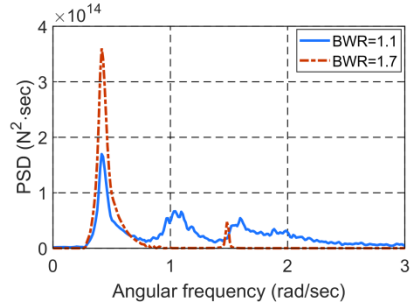(d) Spectrum of shear force in the horizontal direction (VM)

(e) Time series of shear force in the vertical direction (IM))

(f) Spectrum of shear force in the vertical direction (IM)

(g) Time series of shear force in the horizontal direction (IM)

(h) Spectrum of shear force in the horizontal direction (IM)

Fig. 14 Time series of shear force at BWRs of 1.1 and 1.7 and corresponding spectra

(a) Envelope of the maximum bending moment in the vertical direction (VM)

(b) Envelope of the maximum bending moment in the vertical direction (IM)

(c) Envelope of the maximum bending moment in the horizontal direction (VM)

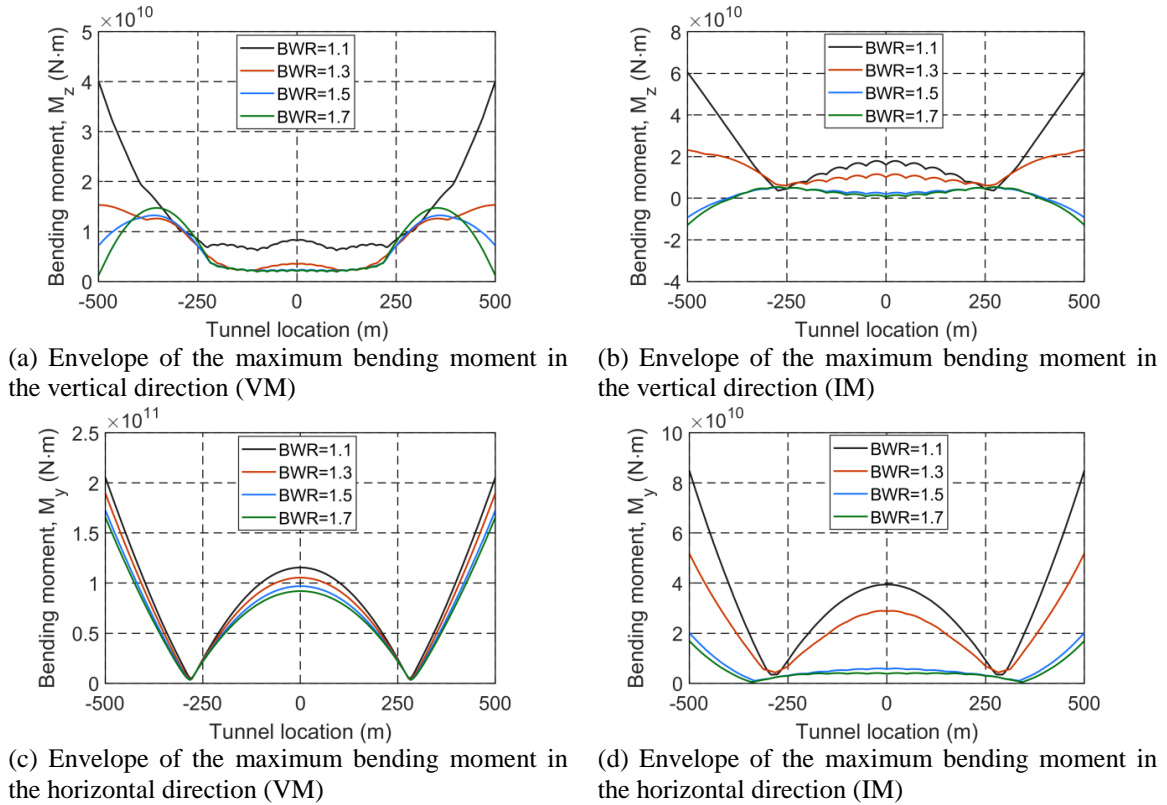(d) Envelope of the maximum bending moment in the horizontal direction (IM)

Fig. 15 Envelopes of bending moment of the tunnel for VM and IM

Fig. 16 shows the times series and spectra of bending moments at the mid-section of the tunnel at BWRs of 1.1 and 1.7. In case of VM, the dynamic bending moments for both directions do not change much by increasing BWR from 1.1 to 1.7. However, in IM case, the dynamic bending moments for both directions decrease significantly by increasing BWR from 1.1 to 1.7. Therefore, for any given design, the gain or loss, both statically and dynamically, by varying BWRs should be carefully investigated to find the optimal value.

Finally in Fig. 17, we plotted the horizontal and vertical accelerations at the mid-section of the SFT for both VM and IM with BWR=1.3. It is seen that IM has smaller horizontal accelerations but greater vertical accelerations than VM. Those accelerations are critical for the safety of transportation and people's comfort level although this survival condition is not necessarily the maximum operational condition.

5. Conclusions

Dynamic and structural analyses of a circular SFT under extreme wave excitations are performed using a floater-mooring coupled dynamics simulation program in time-domain. The irregular waves of 100-yr storm were used as inputs. Two different configurations of mooring lines, VM (interval=25 m) and IM (interval=50 m), are considered with varying submergence depths and
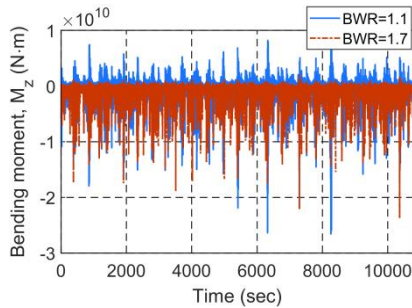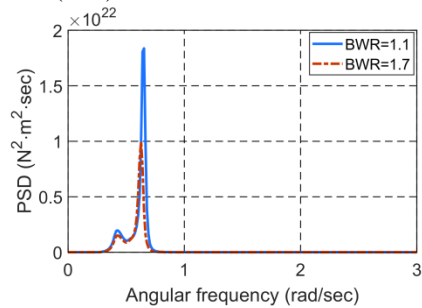
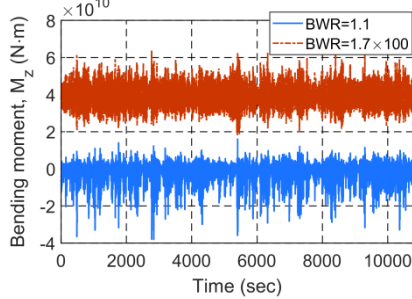(a) Time series of bending moment in the vertical direction (VM)
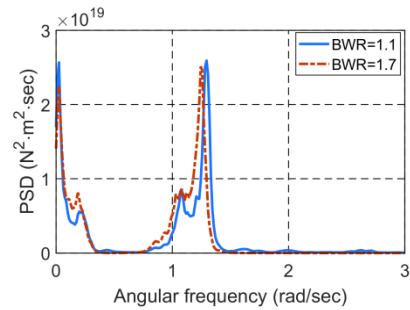
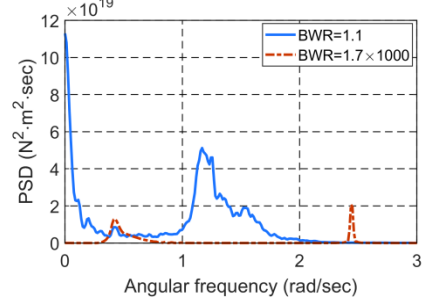(b) Spectrum of bending moment in the vertical direction (VM)
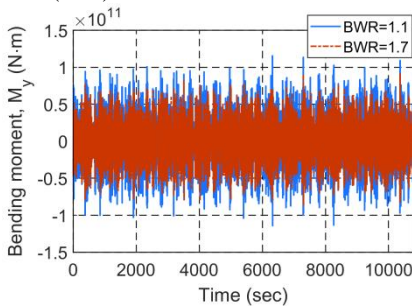
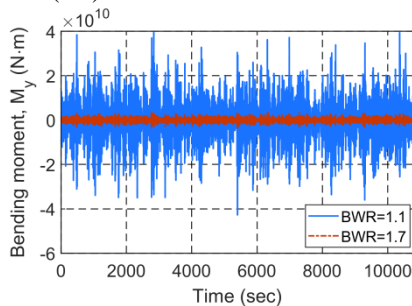(c) Time series of bending moment in the horizontal direction (VM)

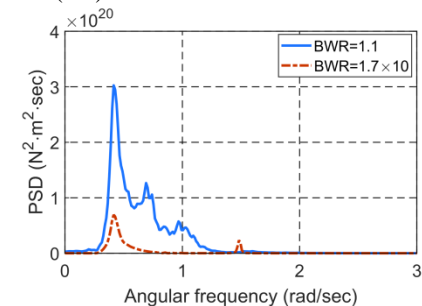(d) Spectrum of bending moment in the horizontal direction (VM)

(e) Time series of bending moment in the vertical direction (IM)

(f) Spectrum of bending moment in the vertical direction (IM)

(g) Time series of bending moment in the horizontal direction (IM)

(h) Spectrum of bending moment in the horizontal direction (IM)

Fig. 16 Time series of bending moment at the BWR of 1.1 and 1.7 and corresponding spectra

(a) Time series of horizontal acceleration (VM)

(b) Time series of horizontal acceleration (IM)

(c) Time series of vertical acceleration (VM)
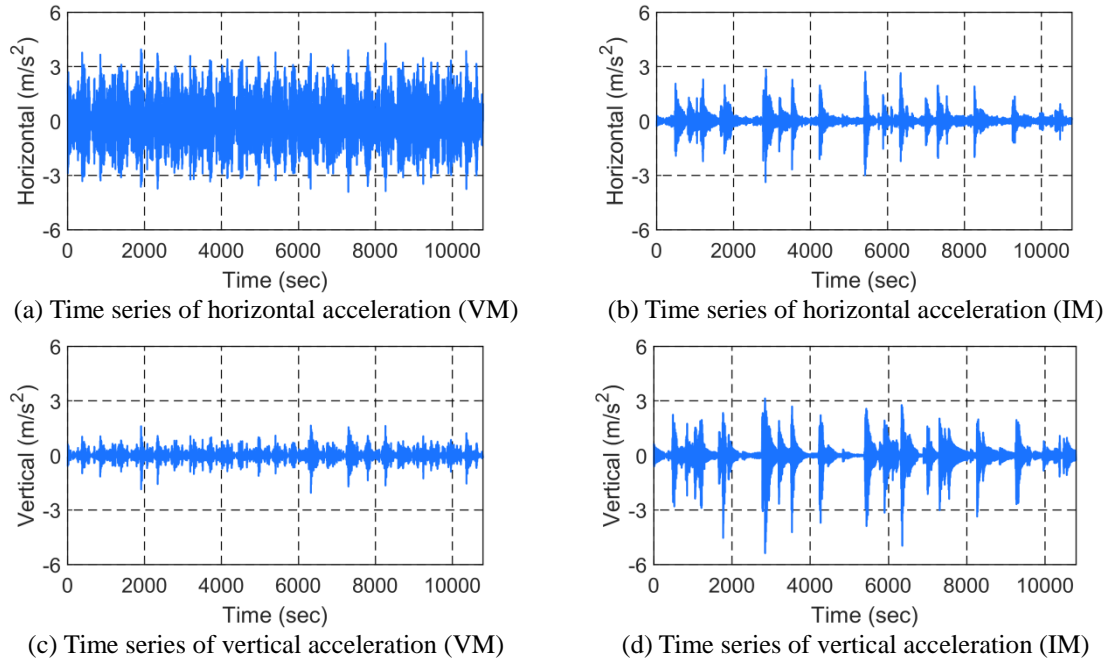
(d) Time series of vertical acceleration (IM)

Fig. 17 Time series of horizontal and vertical acceleration at the BWR of 1.3

BWR=1.1, 1.3, 1.5, and 1.7. Modal analysis is conducted to obtain the corresponding wet natural frequencies and mode shapes of the entire system clamped at both ends. The max-min envelopes of horizontal/vertical responses, accelerations, mooring tensions, and shear forces/bending moments of the tunnel along the longitudinal (1000-m long) direction are presented in static and dynamic conditions. The maximum elastic responses and tensions for both mooring types occur at the mid-section, while maximum shear forces and bending moments occur at both clamped ends, as expected. In addition, the times series and spectra of vertical/horizontal responses and mooring tensions as well as shear forces/bending moments at the middle section of the tunnel are also evaluated and compared.

In the static condition, the BWR is the main parameter to determine the static displacement in vertical direction, which leads to the variations of not only mooring tensions but also shear forces and bending moments. As BWR increases, the maximum values of those parameters also rise.

In the dynamic condition, horizontal responses of VM are larger than those of IM since the horizontal stiffness of VM is smaller and its lowest natural frequency is closer to the incident wave frequencies. The vertical responses of VM are predominantly downward and also caused by set-down effects. When bouncing back from the slack mooring condition caused by large vertical downward motion, the mooring lines experience sharply increased snap loading. The increase of submergence depth significantly reduces the overall dynamic effects. At the mid-section, the maximum dynamic shear forces and bending moments generally increase with decreasing BWR but exceptions may happen, such as the horizontal shear force in VM, due to the increased inertia effect with high BWR. Therefore, for any given design, the static/dynamic gain or loss by varying BWRs, boundary conditions, and mooring types should be carefully investigated to find the optimal values. Through the present study, it is well demonstrated that the time-domain numerical

simulation of the real system including nonlinear hydro-elastic dynamics coupled with nonlinear mooring dynamics is a good method to determine various design parameters.

Acknowledgments

References

Chamelia, D.M., Wardhana, W. and Prastianto, R.W. (2015), "Dynamic response analysis on submerged floating tunnel due to hydrodynamic loads", *Procedia Earth Planetary Sci.*, **14**, 220-227.

Cifuentes, C. and Kim, M.H. (2017), "Numerical simulation of fish nets in current using a morison force model", *Ocean Syst. Eng.*, **7**(2), 143-155.

Cifuentes, C., Kim, S., Kim, M.H. and Park, W.S. (2015), "Numerical simulation of the coupled dynamic response of a submerged floating tunnel with mooring lines in regular waves", *Ocean Syst. Eng.*, **5**(2), 109-123.

Di Pilato, M., Perotti, F. and Fogazzi, P. (2008), "3d dynamic response of submerged floating tunnels under seismic and hydrodynamic excitation", *Eng. Struct.*, **30**(1), 268-281.

DNV (2010), Position Mooring, Offshore Standard DNV-OS-E301, 1-100.

ESDU (1980), Mean Forces, Pressures and Flow Field Velocities for Circular Cylindrical Structures: Single Cylinder with Two-Dimensional Flow, ESDU 80025, 1-60.

Faggiano, B., Landolfo, R. and Mazzolani, F. (2001), "Design and modelling aspects concerning the submerged floating tunnels: An application to the messina strait crossing", *Proceeding of the 3rd International Conference on Strait Crossing*, Bergen, Norway.

Faltinsen, O. (1993), *Sea Loads on Ships and Offshore Structures*, Cambridge university press.

Fujii, T. (1996), "Submerged floating tunnels project in Funka Bay design and execution", *Proceedings of the International Conference on Submerged Floating Tunnel*, Sandnes, Norway.

Ge, F., Lu, W., Wu, X. and Hong, Y. (2010), "Fluid-structure interaction of submerged floating tunnel in wave field", *Procedia Eng.*, **4**, 263-271.

Ghimire, A. and Prakash, O. (2017), "Intangible study for the design and construction of submerged floating tunnel", *Imperial J. Interdisciplinary Res.*, **3**(4), 721-723.

Hong, Y. and Ge, F. (2010), "Dynamic response and structural integrity of submerged floating tunnel due to hydrodynamic load and accidental load", *Procedia Eng.*, **4**, 35-50.

Indridason, B. (2013), Earthquake Induced Behavior of Submerged Floating Tunnels with Tension Leg Anchorage, M.S., Thesis, NTNU.

Jin, C.K., Lee, J.Y., Kim, H.S. and Kim, M.H. (2017), "Dynamic responses of a submerged floating tunnel in survival wave and seismic excitations", *Proceedings of the 27th International Ocean and Polar Engineering Conference*, San Francisco, USA.

Kim, M. and Yue, D. (1991), "Sum and difference-frequency wave loads on a body in unidirectional Gaussian seas", *J. Ship Res.*, **35**(2), 127-140.

Kunisu, H., Mizuno, S., Mizuno, Y. and Saeki, H. (1994), "Study on submerged floating tunnel characteristics under the wave condition", *Proceedings of the 4th International Offshore and Polar Engineering Conference*.

Lee, J.Y., Jin, C.K. and Kim, M.H. (2017), "Dynamic response analysis of submerged floating tunnels by wave and seismic excitations", *Ocean Syst. Eng.*, **7** (1), 1-19.

Long, X., Ge, F., Wang, L. and Hong, Y. (2009), "Effects of fundamental structure parameters on dynamic responses of submerged floating tunnel under hydrodynamic loads", *Acta Mechanica Sinica*, **25**(3), 335-344.

Longridge, J., Randall, R. and Zhang, J. (1996), "Comparison of experimental irregular water wave elevation and kinematic data with new hybrid wave model predictions", *Ocean Eng.*, **23**(4), 277-307.

Lu, W., Ge, F., Wang, L., Wu, X. and Hong, Y. (2011), "On the slack phenomena and snap force in tethers of submerged floating tunnels under wave conditions", *Mar. Struct.*, **24**(4), 358-376.

Mazzolani, F., Landolfo, R., Faggiano, B., Esposto, M., Perotti, F. and Barbella, G. (2008), "Structural analyses of the submerged floating tunnel prototype in Qiandao Lake (Pr of China)", *Adv. Struct. Eng.*, **11** (4), 439-454.

Oh, S.H., Park, W.S., Jang, S.C., Kim, D.H. and Ahn, H.D. (2013), "Physical experiments on the hydrodynamic response of submerged floating tunnel against the wave action", *Proceedings of the 7th International Conference on Asian and Pacific Coasts*, Bali, Indonesia.

Orcina (2015), Orcaflex Manual Version 9.8a, Orcina.

Paik, I.Y., Oh, C.K., Kwon, J.S. and Chang, S.P. (2004), "Analysis of wave force induced dynamic response of submerged floating tunnel", *KSCE J. Civil Eng.*, **8**(5), 543-550.

Remseth, S., Leira, B.J., Okstad, K.M., Mathisen, K.M. and Haukås, T. (1999), "Dynamic response and fluid/structure interaction of submerged floating tunnels", *Comput. Struct.*, **72**(4), 659-685.

Seo, S.I., Mun, H.S., Lee, J.H. and Kim, J.H. (2015), "Simplified analysis for estimation of the behavior of a submerged floating tunnel in waves and experimental verification", *Mar. Struct.*, **44**, 142-158.

Skorpa, L. (1989), "Innovative Norwegian Fjord crossing. how to cross the Høgsjord, alternative methods", *Proceedings of the 2nd Congress Marine and Offshore Engineering Association*, Naples, Italy.

Wahyuni, E., Budiman, E. and Raka, I.G.P. (2012), "Dynamic behaviour of submerged floating tunnels under seismic loadings with different cable configurations", *IPTEK*, **23**(2), 82.

Wheeler, J. (1969), "Methods for calculating forces produced by irregular waves", *Offshore Technology Conference*, 1-12.

PL